Coherent and incoherent Rayleigh wave attenuation for discriminating microstructural effects of thermal damage from moisture conditions in concrete

Massina Fengal, Pierric Mora, Parisa Shokouhi, Olivier Durand, Xavier Dérobert, Sérgio Palma-Lopes, Maximilien Lehujeur, Géraldine Villain, Eric Gennesseaux, Odile Abraham

▶ To cite this version:

Massina Fengal, Pierric Mora, Parisa Shokouhi, Olivier Durand, Xavier Dérobert, et al.. Coherent and incoherent Rayleigh wave attenuation for discriminating microstructural effects of thermal damage from moisture conditions in concrete. NDT & E International, 2025, 156, pp.103473. ⟨10.1016/j.ndteint.2025.103473⟩. ⟨hal-05443536⟩

HAL Id: hal-05443536
https://hal.science/hal-05443536v1

Submitted on 8 Jan 2026

NDT&E International 156 (2025) 103473

Contents lists available at ScienceDirect

NDT and E International

journal homepage: www.elsevier.com/locate/ndteint

Research Paper

Coherent and incoherent Rayleigh wave attenuation for discriminating microstructural effects of thermal damage from moisture conditions in concrete

Massina Fengal [a,*], Pierric Mora [a], Parisa Shokouhi [d], Olivier Durand [a], Xavier Dérobert [a], Sérgio Palma-Lopes [a], Maximilien Lehujeur [a], Géraldine Villain [b], Eric Gennesseaux [c], Odile Abraham [a]

[a] *GERS-GeoEND, Univ Gustave Eiffel, Campus de Nantes, F-44344 Bouguenais, France*
[b] *MAST-LAMES, Univ Gustave Eiffel, Campus de Nantes, F-44344 Bouguenais, France*
[c] *MAST-MIT, Univ Gustave Eiffel, Campus de Nantes, F-44344 Bouguenais, France*
[d] *The Pennsylvania State University, University Park, PA 16801, United States*

ARTICLE INFO

Keywords:
Ultrasonic testing
Cementitious materials
Post-fire curing recovery
Attenuation by scattering
Attenuation by absorption
Capacitance
DC-resistivity
Mortar

ABSTRACT

Thermal damage results in a depth-dependent variation in concrete mechanical properties, which is commonly investigated by invasive sampling and destructive testing. Ultrasonic Rayleigh wave (R-wave) testing offers a non-destructive alternative for mapping mild to moderate thermal damage in cementitious materials. However, the coupled influence of damage and moisture gradients on the ultrasonic measurements is not known, while it is known that rehydration causes partial recovery of mechanical properties. In this study, we prepare concrete and mortar blocks subjected to two distinct heating scenarios: a short-duration high-temperature exposure following the ISO fire standards, and a lower-intensity longer heating using radiant panels. We then use P-wave refraction, R-wave phase velocity and attenuation and diffuse field analysis to test the exposed blocks first at ambient conditions and later after water saturation, in order to decouple the influence of water saturation from that of thermal damage. The ultrasonic results are interpreted in relation to other non-destructive measurements: resistivity and capacitance. We find that although R-wave phase velocity is indeed sensitive to thermal damage, it is also significantly affected by the effect of moisture as it can hardly distinguish between exposed and intact surfaces after post-fire re-curing. In contrast, coherent R-wave attenuation effectively discriminates a damaged surface. The distinct analysis of coherent and incoherent attenuation enables to separate the impacts of thermal damage and moisture content. Overall, this article highlights the potential of attenuation for assessing damage under unknown moisture conditions.

1. Introduction

Concrete is widely used in construction because of its strength and durability. However, its advantageous mechanical properties can be compromised in service by various forms of environmental or accidental factors, such as thermal exposure [1]. In particular, thermal exposure creates a thermal gradient throughout the material, leading to depth-dependent variations in concrete properties [2]. The effects of elevated temperatures on concrete are well documented [3,4] and include both chemical and physical changes depending on the temperature level. Traditionally, assessing these changes requires invasive sampling and destructive testing [5]. Non-destructive evaluation (NDE) methods provide an alternative for assessing these alterations; however, their assessment can be influenced by other factors such as moisture gradients. Non-destructive profiling of material property gradients often involves surface measurements tuned to inspect various depths. For instance, the propagation of Rayleigh wave (R-wave) is primarily affected by the mass density and shear modulus of the test medium, the probing depth is controlled by the excitation frequency [6]. If the P-wave velocity increases with depth, measuring the travel time of the refracted P-wave as a function of the distance from the source allows for the inversion of the velocity profile [7,8]. Direct Current resistivity (DC-resistivity) measurements, which are sensitive to ions concentration present in poral space, measure apparent resistivity between electrodes disposed on the surface; by adjusting the distance

---

[*] Corresponding author.
E-mail address: massina.fengal@univ-eiffel.fr (M. Fengal).

https://doi.org/10.1016/j.ndteint.2025.103473
Received 7 February 2025; Received in revised form 15 May 2025; Accepted 15 June 2025

between the electrodes, the depth of investigation can be tuned [9]. Capacitive measurements, sensitive to volumetric water content, rely on the sensor's geometry, allowing for different electrode configurations to achieve varying inspection depths [10].

Previous research has investigated the impact of water content on NDE measurements in concrete, often assuming uniform saturation throughout the sample, without addressing surface gradients. As water content increases, resistivity decreases [11,12], and capacitance increases [13], while ultrasonic wave velocities and attenuation show varying trends depending on the material examined and water saturation level. While there is a consensus that near-total water saturation generally leads to higher ultrasonic velocities, the observations differ for partially saturated materials. Some studies report a U-shaped trend for wave velocities as water saturation rises [14–16], while others report a monotonic increase [17–19] with P-waves being particularly sensitive. The assumption of homogeneous moisture content was challenged in [14], which demonstrates that R-wave velocities decrease for larger wavelength (deeper) in fully water saturated concrete, showing a pronounced dispersion even in saturated conditions. Wave attenuation vs. water saturation exhibits a bell-shaped pattern [14]. However, accurate measurement of attenuation is notoriously challenging and requires a significant number of spatial averages to minimize the contributions of the incoherent field [6]. Consequently, the attenuation vs. water content relationship is less investigated.

This paper investigates the coupled influence of damage and water saturation gradients on ultrasonic testing of concrete and mortar blocks. These blocks were first exposed to elevated temperatures for a short period of time, stored under ambient laboratory conditions for several months, and then immersed in water. Multiple independent surface measurements were carried out using a home-made dry-contact multi-element ultrasonic probe to enhance accuracy and minimize noise. Material properties extracted from ultrasonic measurements are compared with those from electromagnetic testing, namely capacitance and DC-resistivity techniques, which help compare moisture contents at initial stage, follow the kinetics of water saturation and re-curing, and identify porosity gradients caused by the exposure. In particular, we show that attenuation analysis provides two complementary pieces of information: the effects of damage on the microstructure through coherent field analysis and the presence of moisture content through incoherent field analysis.

2. Materials and methods

The experimental procedure involved the preparation of ordinary concrete and mortar blocks, followed by exposure to thermal treatments using both ISO standard fire exposure and radiant panels. Non-destructive evaluation techniques, including ultrasonic measurements, capacitive, and DC-resistivity testing, were employed on the samples. The non-destructive tests were repeated during and after water saturation.

2.1. Materials

In this section, the specimens of the study are presented. The material mixes, and the mechanical properties obtained from the 28-day compression tests, are first detailed. Then, the thermal damage applied to the specimens is discussed in relation to what is known in the literature. Finally, the imbibition saturation protocol and the monitoring of saturation are outlined. Fig. 1(c) summarizes the global timeline of the specimens preparation.

Table 1
Concrete and mortar composition kg/m^3.

	Cement	Sand	Aggregate	w/c
Concrete	350	890	984	0,59
Mortar	538	1367	0	0,59

2.1.1. Preparation

Four specimens were prepared: two concrete blocks and two mortar blocks, each with dimensions of 50 × 25 × 12 cm^3. The concrete mix consisted of CEM I 52.5 N SR3 cement, admixtures, 0/4 mm sand, 4/12 mm limestone aggregates, and a water-to-cement ratio w/c of 0.59 (see Table 1), densities of $2395 \pm 3\ \text{kg/m}^3$ for the concrete and $2262 \pm 5.7\ \text{kg/m}^3$ for the mortar. Then, the blocks and five standardized cylindrical specimens, each measuring 11 cm in diameter and 22 cm in height, underwent 28 days of water curing. The compressive strength at 28 days conducted on standardized cylindrical specimens, as per the NF EN 12390-3 standard, was 42.4 ± 0.3 MPa for concrete and 40.8 ± 1.3 MPa for mortar.

It is well established that the casting process itself creates an initial near surface properties gradient in the material due to the wall effect [6,20,21]. The wall effect in concrete refers to the uneven distribution of aggregates caused by the presence of formwork (mould blocks). Our blocks were cast vertically from the face of size 25 x 12 cm^2, *i.e.* the wall effect affects the faces where non-destructive measurements are conducted. This effect perturbs the particle distribution by repelling larger aggregates [20], which furthermore tend to act as a barrier to smaller, nearby aggregates [21]. This results in a predominance of small particles and an increase of the porosity near the boundaries, and a higher concentration of larger particles inside the element, and in turn in lower wave velocities near the surface [6,22]. The depth of this wall effect is a function of the volume ratio of aggregates to the total volume and the maximum size of the aggregates (Eq. (9)-c in [20]). In our case, this results in a depth of approximately 9.6 mm for concrete and of approximately 2.5 mm for mortar.

2.1.2. Thermal exposures and damage due to temperature

For each set of material, one block is exposed to temperature on one side (50 x 25 cm^2), while the other block is kept as a reference, as represented in Fig. 1(a). The test specimens underwent two specific heat treatments, carefully designed to create varying temperature gradients within the top few centimetres beneath the surface. The first heat treatment was aimed to establish a strong temperature gradient near the surface. It consisted of a 20 min exposure to a fire in accordance with ISO fire standards and resulted in an increase of the temperature from ambient to 370 °C at the surface and to 130 °C at a depth of 3 cm. In contrast, the second treatment was aimed to produce a milder and more penetrating temperature increase. It consisted in a 1-hour exposure to radiant panels and resulted in an increase of the temperature from ambient to 240 °C at the surface and to 135 °C at a depth of 3 cm. Fig. 1(b) presents the temperature curves recorded by five thermocouples positioned at various depths during the heating phase and subsequent cooling under ambient temperature conditions.

The effects of high-temperature exposure on concrete are well documented and can be categorized into two main types: physical and chemical changes [23–26]. The former refers to physical damage, including mass loss due to the evaporation of free water and the formation of cracks resulting from the pressure caused by water migration, as well as cracks induced by the differing thermal expansion rates of the cement mortar matrix and aggregates. The latter pertains to chemical changes, which include the decomposition of both the hardened cement matrix and the aggregates.

Crack formation is partially attributed to the evaporation of free water [23]. As the temperature rises, free water near the heated surface evaporates rapidly, leading to a reduction in moisture content and the

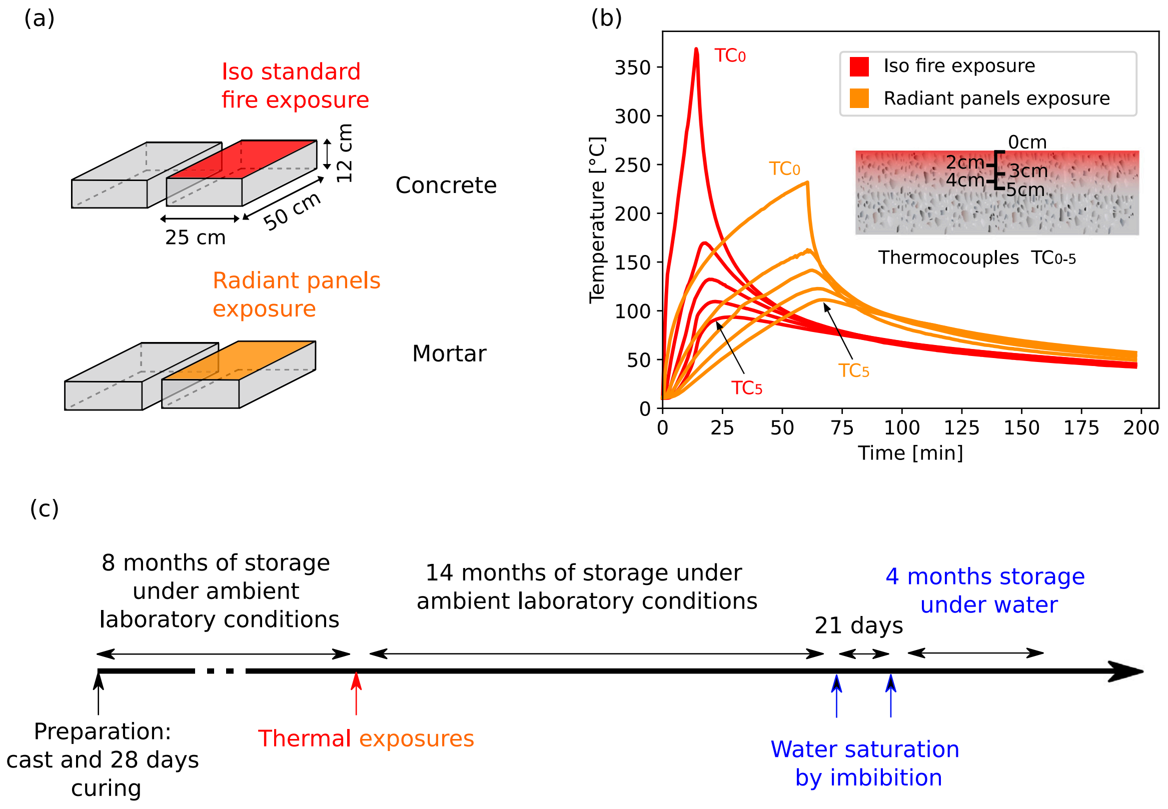

Fig. 1. Experimental setup: (a) Specimens of the study; (b) Temperature curves recorded by the five thermocouples for the two distinct types of damage. The thermocouples TCi i=0,1,2,3,4 and 5 are placed at depths of 0, 2, 3, 4, and 5 (cm) respectively beneath the exposed surface; (c) global timeline of the specimens preparations.

development of a dry zone. This process creates a moisture imbalance and causes water migration towards cooler regions within the concrete (deeper in the material). The water trapped in the pores generates increasing pressure due to its inability to escape quickly. When the vapour pressure exceeds the concrete's tensile strength, microcracks form. The faster heating rate during the ISO fire (17.5 °C/min) compared to the radiant panel exposure (3.6 °C/min) produces higher pressures due to the evaporation of free water in concrete, resulting in the formation of more cracks.

Cracks also form due to the different thermal expansion rates between the cement paste and the aggregates. The difference in thermal properties between the mortar matrix and the aggregates induces thermal stresses and possibly cracking in the concrete. Three types of thermal cracks have been identified: radial cracks (between two neighbouring aggregates), tangential cracks (in the aggregate-mortar matrix interfacial zones) and aggregate cracks. The formation and propagation of these cracks depend on the difference in the CTE (coefficient of thermal expansion) between the aggregates and the mortar matrix. The average CTE of aggregates, primarily limestone in this study, $CTE_A \approx 6\text{–}13\,\mu\varepsilon\,{}^{\circ}\mathrm{C}^{-1}$ [27], is less than that of the cement matrix, $CTE_{CM} \approx 126\text{–}26\,\mu\varepsilon\,{}^{\circ}\mathrm{C}^{-1}$ [28]. Numerical [24] and experimental [25] studies have shown that in this case, tangential cracks are formed along the interface between the matrix and the inclusion. The presence of aggregates in concrete intensifies the thermal expansion mismatch between aggregates and the cement paste, leading to more severe cracking compared to mortar.

The chemical process of thermally damaged concrete is well known and described in [26]. The main chemical process responsible for the internal damage of concrete is the alteration of hydrates. A series of transformations occurs during heating, beginning with the dehydration of ettringite at 80°C. The transformation of C-S-H occurs between 180°C and 300°C, while the dehydration of calcium hydroxide starts, with the decomposition of portlandite initiating at 400°C. The first chemical transformation in aggregates, specifically the quartz phase change, takes place at 570°C, though this is not relevant to the present case study. In concrete, exposure to the ISO standard fire reaches approximately 370 °C, while the radiant panels exposure in mortar reaches only around 240 °C. This temperature difference affects the level of dehydration in the two materials.

The overall timeline of specimen preparation is presented in Fig. 1(c). Measurements under ambient moisture conditions were performed during a 14-month storage period under controlled laboratory conditions. The laboratory temperature was maintained between 18 °C and 22 °C, with a relative humidity estimated between 30% and 40%. Ultrasonic measurements were performed at 8 months into this storage period. The results did not show any significant variability, indicating that ambient storage conditions had no notable impact on the analysis.

2.1.3. *Water saturation*

After being subjected to thermal damage, the blocks underwent a saturation process through imbibition. The intact surfaces of the blocks were placed in a water tank, initially submerged to a depth of 3 cm, as shown in Fig. 4(a). The water level was gradually increased by 3 cm each week until the blocks were fully submerged. The saturation process was monitored by periodically measuring the mass of the blocks and conducting all the other NDE measurements, first on a weekly basis and then less frequently. The protocol and results of the multiphysics monitoring, including mass gain, ultrasonic Rayleigh wave phase velocity and coherent attenuation measurements, as well as capacitive measurements, are presented in Fig. 4. Fig. 4(b-c) illustrates the mass gain of the blocks throughout the imbibition process, showing that the concrete block absorbed $\approx 1.1\,\mathrm{kg}$ of water and the mortar block absorbed $\approx 1.8\,\mathrm{kg}$. It is also noted that between the 21st and 114th day, when the blocks were fully submerged in water, the concrete, and mortar mass blocks gained additional grams.

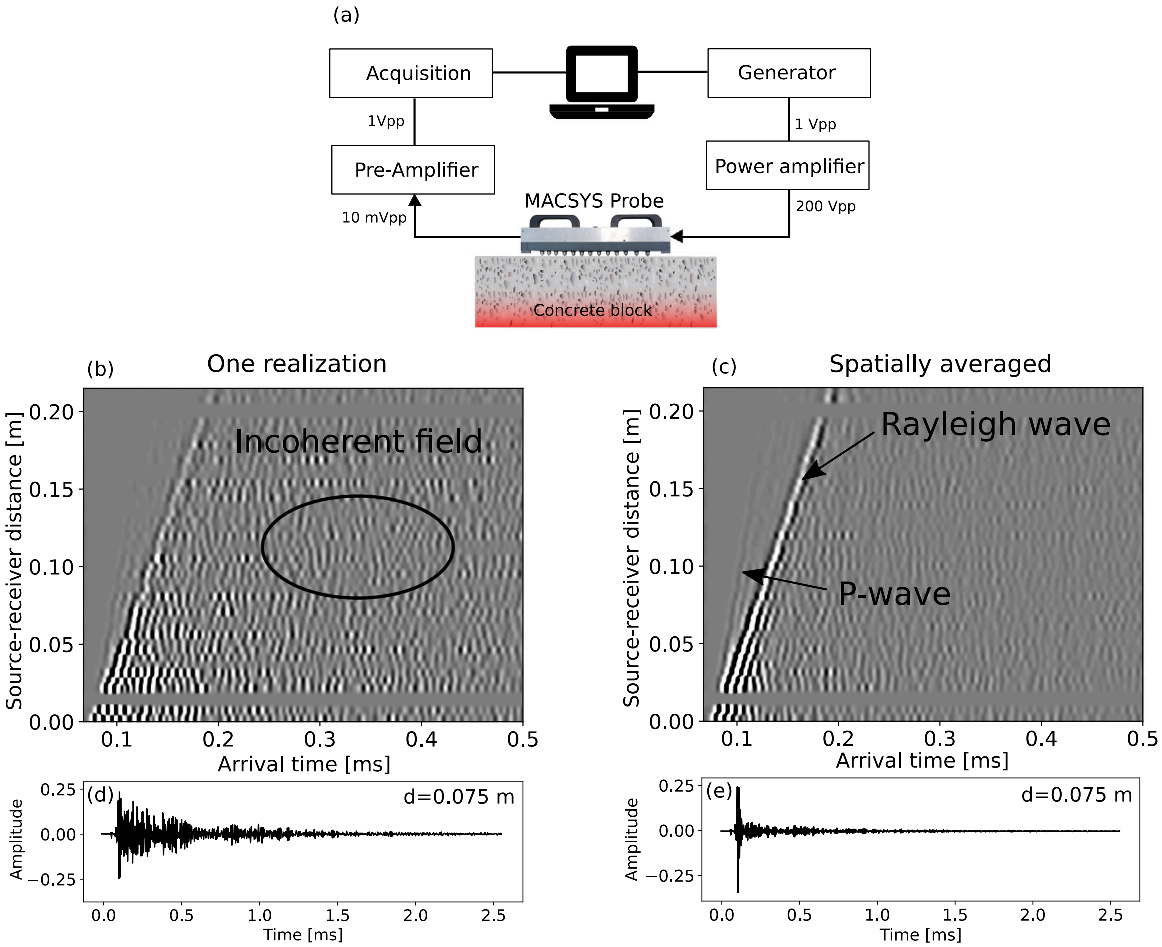

Fig. 2. Experimental ultrasonic measurement setup and representative raw data: (a) experimental setup using a custom-made Macsys probe; (b) B-scan obtained at a specific location on the intact concrete surface; (c) averaged B-scan from 25 measurements at different locations on the same surface; (d) single trace recorded at a source–receiver distance of 7.5 cm; (e) average of 25 traces recorded at the same distance but at 25 different surface locations.

2.2. NDE methods

This section is divided into two parts. The first part describes the setup, data processing, and inversion procedures for ultrasonic measurements, including Rayleigh wave attenuation, phase velocity, and time-of-flight measurements of refracted longitudinal waves, all of which will be inverted. The second part focuses on electromagnetic measurements, including capacitive and DC-resistivity measurements.

2.2.1. Ultrasonics measurements

The experimental setup uses a home-made dry-contact multi-element ultrasonic probe, as shown in Fig. 2(a). This probe consists of 13 Acsys P-wave S1803 transducers. The transducers are arranged to simulate 1 source and 40 receivers located 25 mm to 240 mm from the source, with a 5 mm spacing. A chirp signal is emitted between 15 and 480 kHz and correlated with the measured signals to simulate a Ricker wavelet with a central frequency of 120 kHz. Two thousand temporal averages are taken to achieve a suitable signal-to-noise ratio for the P-wave. Additionally, 50 measurements are conducted at different probe positions on the surface of the block, allowing for the mitigation of incoherent wave fields through spatial averaging [6]. An example of a B-scan for an intact concrete surface under ambient environmental conditions is shown in Fig. 2(b) for one measurement location. Fig. 2(e) shows the average B-scan resulting of 25 measurements at different locations on the surface of the block. Fig. 2(d) and (e) display an example of the measured signal at a source-receiver distance of 7.5 cm for one measurement location, and the spatially averaged results, respectively.

The use of coherent and incoherent fields allows us to measure four parameters. From the coherent field, we measure (1) the Rayleigh wave (R-wave) phase velocity, (2) the attenuation, and (3) the direct and refracted P-wave velocities. From the incoherent field, we measure (4) the attenuation caused by material damping.

The 50 data measurements are used to define 5 averaged datasets, each one consisting of 25 randomly chosen measurements. For each averaged data set, the R-wave phase velocity dispersion curve is extracted using a $p-\omega$ transform [29], and the attenuation factor is estimated from the decrease in the amplitude spectrum of the coherent field after correction of the geometric attenuation. The final curves represent the average of the 5 curves resulting from the random selections.

The dispersion curves are inverted to infer the 1D S-wave velocity profile using a Monte Carlo approach, as in [30]. Additionally, a cost term was introduced to penalize the norm of the gradient of the parameters with depth (Tikhonov regularization [31]).

The inversion method requires, as input, a dispersion curve with its associated uncertainty. The uncertainty of the dispersion curve is estimated as the sum of two main sources. The first source is related to the $p-\omega$ transform, which considers the lobe width and is evaluated using the relationship $\frac{c}{f\times L}$ [32], where c represents the phase velocity, f the frequency, and L the measurement line length. The second source of uncertainty arises from the material heterogeneity and is defined here as the standard deviation among the five randomly selected dispersion curves. The final inversion result considered is the median of the 1000 best solutions. An example of the results is shown in Appendix A.

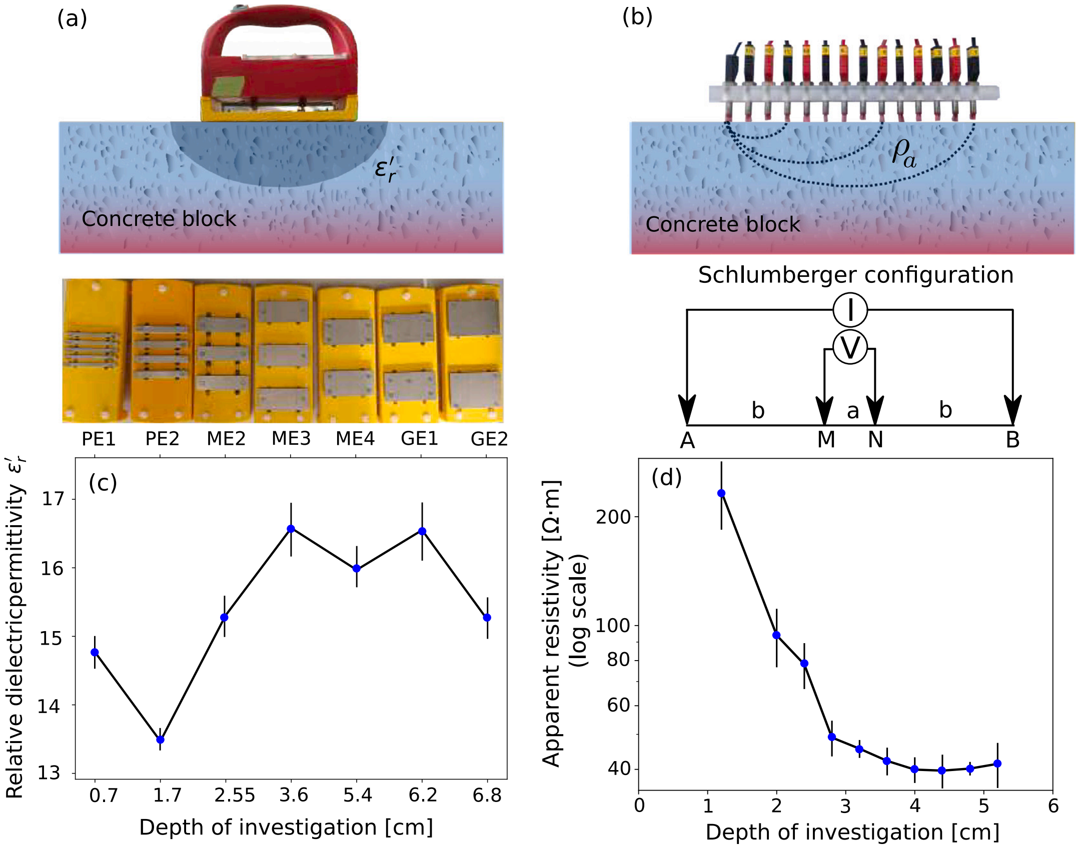

Fig. 3. Experimental setup for electromagnetic measurements: (a) Capacitive measurement system with seven different electrode arrays. (b) A 14-electrode probe for DC-resistivity measurements, including a schematic of the Schlumberger electrode configuration, where a and b represent the electrode spacings, A and B are the injection electrodes, and M and N are the measurement electrodes. (c) and (d) show the raw measurement results of relative dielectric permittivity and apparent resistivity for an intact surface of the concrete block under water saturation after 88 days cure. Error bars for the capacitive measurements indicate the standard deviation of the mean of nine measurements taken at the central area of the surface, while error bars for resistivity measurements represent the standard deviation of the mean for measurements taken at the same depth level in the Schlumberger configuration.

First-arrival picking was performed on the same dataset, with flight times determined as the average from 50 data measurements. The resulting curves were then fitted using a bi-layer refraction model. The fitting procedure, along with an application example on an intact concrete block under ambient temperature, is shown in Appendix B.

The attenuation of the incoherent field of the signal is extracted from the evolution of the diffuse energy, which occurs on a much longer timescale than the time necessary for the coherent wave to propagate. The received data were first processed using time-frequency analysis (Short Time Fourier Transform) with a window duration of 8 μs. The mean energy $< E(f,t,d) >$ at a given source-receiver distance d was then obtained by averaging these (squared) band-passed signals over the 50 measurements. The incoherent attenuation is finally determined by fitting an exponential decrease to the long-time decay ($t > 0.5$ ms), after averaging $\langle E \rangle$ over d.

2.2.2. Electromagnetic measurements

Capacitive measurements assess the relative dielectric permittivity of concrete, denoted by ε_r'. It is also referred to as “apparent”: it is the permittivity of a homogeneous medium whose capacitance measurement is the same as that of the medium being tested. This parameter quantifies the material’s ability to store electrical energy when subjected to an external electric field [33]. Relative dielectric permittivity is represented by the real part of a complex value, which depends on the oscillation frequency and the polarization of the electric field.

The real component accounts for polarization effects, while the imaginary part reflects energy losses [10]. Measurements are performed on the material’s surface using various probes configured as coplanar capacitors, differing in electrode number and spacing to adjust the depth of investigation [13] (see Fig. 3-a). Each of the capacitive probes used in this study is connected to a resonant circuit with an oscillator operating at 33 MHz. Calibration is carried out using reference materials with known permittivity, and environmental capacitance is accounted for by referencing measurements taken in air. Each measurement sequence provides nine surface values, and the error on the average of these measurements for each probe is shown in Fig. 3-(c). This figure illustrates an example of results obtained on an intact concrete surface under water-saturated conditions. Capacitive measurements were conducted on intact and damaged surfaces of concrete and mortar blocks following thermal exposures, both under ambient moisture conditions and after water saturation.

DC-resistivity in concrete evaluates the material’s resistance to the flow of electric charges, denoted as ρ_a (Ω m) [33]. Measurements are conducted using a four-electrode method in Schlumberger configuration with variable spacing [33]. The probe was connected to a multichannel resistivity metre (Iris Instruments Syscal Pro) enabling rapid measurement at low frequency (2 Hz). The resistivity probe comprises 14 electrodes spaced at 20 mm intervals, enabling depth profiling based on electrode separation [9]. The probe and the measurement scheme are shown in Fig. 3-(b). Each measurement sequence yields 67 apparent resistivity values. The results take into account the geometric effect through a factor calculated using a Finite Element model. The investigation depths correspond to the maximum length of the Schlumberger configuration during the measurements, denoted as $L = AB$, ranging from 6 to 26 cm. This provides 10 investigation depth levels, as shown in Fig. 3-(d). These depths are considered at 20% of the total length of the four-electrode configuration [34]. The error bars represent the standard deviation of the mean of measurements of each depth level. DC-resistivity measurements were conducted on intact and damaged surfaces of concrete and mortar blocks following thermal exposures, but only after water saturation. Under ambient moisture conditions, the surface was too dry to inject sufficient current for measurements.

3. Results and discussion

This section presents the acquired multiphysical data. It first covers water saturation monitoring, then electromagnetic test results, and finally ultrasonic testing findings.

3.1. Water saturation monitoring

The capacitive imbibition monitoring shown in Fig. 4(d-e) is obtained using a probe with a numerically estimated investigation depth of 6.8 cm [13]. On day 0 (before saturation), it can be observed that the value of ε'_r is similar for intact and exposed surfaces. This indicates a nearly identical volumetric moisture content between them, likely due to the storage of samples under ambient laboratory conditions for several weeks without protection. Then, ε'_r increases significantly between day 0 and day 21, indicating substantial water uptake. After day 21, the ε'_r values stabilize, suggesting that the material is nearing full saturation. It is also noted that after day 21, a slight decrease in ε'_r is observed for the exposed surface to damage. This effect accompanies the slight mass gain noticed after day 21 as well. The most probable reason behind this effect is post-fire re-curing recovery, where the filling of pores and cracks by rehydrated products decreases the porosity [35] and increases the mass. Studies summarized in the review [36] show that after a few days of saturation, water does not just fill the pores but begins to alter the properties of fire-exposed concrete, such as strength and permeability, which can be restored. This phenomenon is known as “post-fire curing recovery”. This recovery primarily occurs through a rehydration mechanism, where compounds like calcium hydroxide (CH) and calcium silicate hydrate (C-S-H) fill cracks and pores. In concrete, the rehydrated products help restore the microstructure by reducing the size and connectivity of fire-induced pores and cracks [37], although cracks may expand in cement paste due to the increase in CH volume [38]. Recovery rates depend on the temperature level reached [39] and vary between concrete and mortar. Concrete generally exhibits more recovery, as thermal-induced cracks around aggregates create space for rehydration products to form [40].

Ultrasonic measurements are sensitive to water content [7,14] but also post-fire curing recovery effects. It was shown in [37] that concrete heated at 400 °C can recover up to 90% of its lost velocity after water post-fire curing. Fig. 4 (f-g) illustrates an increase in Rayleigh ultrasonic phase velocity at a wavelength of $\lambda = 1.5$ cm. This increase continues to occur after day 21 for both concrete and mortar, intact and exposed cases, while trends on the mass and capacitance results indicate nearly fully saturated cases. Similarly, Fig. 4 (h-i) shows that after a slight (concrete) or strong (mortar) increase in the first days, coherent attenuation decreases monotonously after day 21. This behaviour in the ultrasonic results is attributed to the post-fire re-curing recovery effects. The filling of pores and cracks by rehydrated products increases the velocities and reduces scattering, and thereby coherent attenuation. Ultrasonic measurements are also sensitive to thermal damage. Indeed, despite similar water content at day 0, ultrasonic measurements can distinguish between the exposed and intact surfaces. A slight U-shaped effect is observed in the Rayleigh wave velocity, particularly for the exposed surface, during the period from day 0 to day 21. Conversely, a bell-shaped trend is noted in the coherent attenuation curves over the same period. This trend indicates a low water content, and the change in trend occurs at a saturation level of around 30%–40% [14,41].

The ultrasonic measurements presented in the following sections, labelled “saturated”, were taken on the 140th day, while the “saturated” electromagnetic measurements were conducted on the 88th day. Ultrasonic measurement were conducted at 8 month Rayleigh wave phase velocity (Figure a below) and attenuation measurements (Figure b below) were performed eight months apart, showing no significant variability.

3.2. Electromagnetic test results

The relative dielectric permittivity ε'_r is mainly sensitive to changes in the volumetric water saturation level of concrete [42,43], with higher values indicating greater volumetric moisture content. The raw relative dielectric constants are presented in Fig. 5(a)–(b) for concrete and mortar, respectively. Capacitive measurements indicate a nearly identical volumetric water saturation state for specimens under ambient humidity conditions, regardless of whether the concrete or mortar is damaged or intact. This is reflected in an apparent dielectric constant ranging between 7 and 9.

Capacitive measurements, like ultrasonic incoherent attenuation measurements, clearly distinguish between the water-saturated state and the ambient moisture state. It should be noted that the depth of investigation corresponds to an integrated volume across the entire thickness, meaning no conclusions can be drawn regarding gradients with depth. All measurements indicate that the relative dielectric permittivity increases with the depth of the integrated investigation volume. However, a comparison between intact and damaged surfaces can be made using differential analysis.

The difference in capacitive measurements between exposed and intact surfaces is presented in Fig. 6(a). It can be observed that the results under ambient moisture conditions show a positive $\Delta\varepsilon'_r$, indicating slightly higher water content at intact surfaces compared to damaged surfaces. However, the comparison between concrete and mortar (red-black vs. orange-black) is difficult to interpret due to the error bars and the narrow gap between the two curves. In the results obtained after water saturation, $\Delta\varepsilon'_r$ becomes negative, indicating mainly higher volumetric water content at damaged surfaces. This suggests that thermal damage increased the density of microcracks near the surface, and shows that this difference is more pronounced in mortar than in concrete.

The apparent electrical resistivity, ρ_a, is sensitive to changes in the volumetric water content in concrete [42], with higher values indicating lower moisture content. The raw relative apparent resistivity values are presented in Fig. 5(c)–(d) for concrete and mortar, respectively. Measurements under ambient moisture conditions could not be performed due to very high contact resistance, despite localized wetting at the contact interface between the electrodes and the block surfaces.

The apparent resistivity values observed in concrete are higher than those in mortar. This is likely due to the presence of aggregates, which are less porous and electrically more resistant or even insulating. In contrast, their absence in mortar results in a higher proportion of cement paste, leading to greater water absorption. For exposed surfaces subjected to thermal damage (red vs black for concrete and orange vs black for mortar), lower resistivity values are observed for both materials. As with capacitive measurements, these resistivity values integrate the entire volume from the surface, corresponding to the depth of investigation. To better assess the differences caused by thermal damage, differential analysis is more appropriate.

The difference in DC-resistivity measurements between exposed and intact surfaces is presented in Fig. 6(b). It can be observed that the difference is positive, indicating lower resistivity on exposed surfaces due to higher water content. This increase in water content is attributed to the higher density of microcracks caused by thermal damage. The difference approaches zero beyond a depth of investigation of 3 cm,

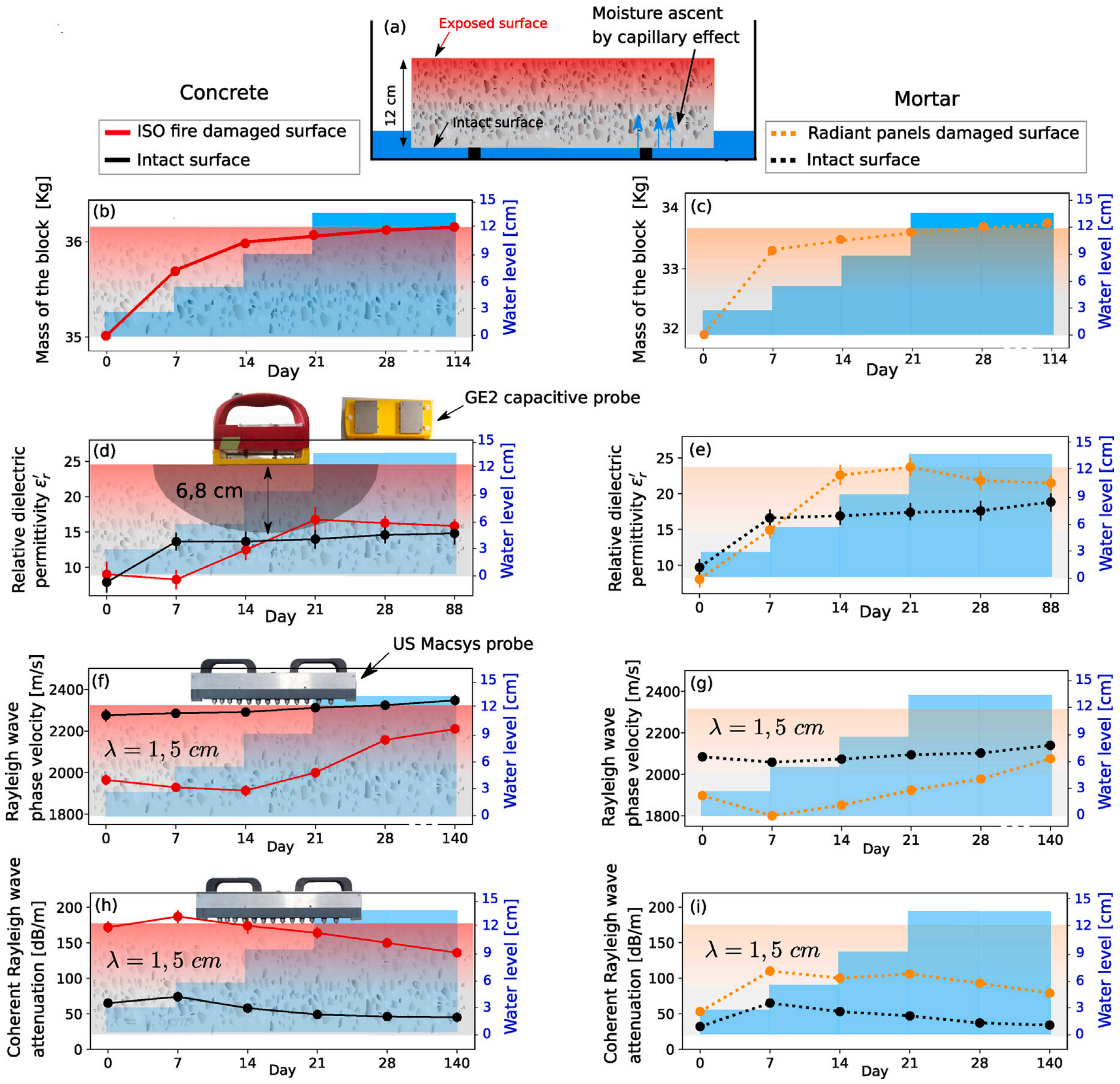

Fig. 4. Monitoring water saturation by imbibition and curing in concrete and mortar blocks from both exposed and intact surfaces: (a) schematic of the immersion process, with the intact surface submerged to a depth of 3 cm during the first week; (b) and (c) show mass gain in concrete and mortar blocks, respectively; (d) and (e) display the relative dielectric permittivity measured using the GE2 capacitive probe, with a penetration depth of 6.8 cm; (f) and (g) illustrate changes in Rayleigh wave phase velocity at $\lambda = 1.5$ cm; (h) and (i) present coherent Rayleigh wave attenuation under the same conditions. Concrete and mortar blocks are shown in each case, respectively.

while it is more significant within the first 3 cm. Furthermore, this effect is more pronounced in concrete compared to mortar.

The comparison of DC-resistivity with the capacitive results is consistent. A low relative dielectric permittivity value is accompanied by high apparent resistivity. Spatially, a differential gradient between surfaces can be observed over the first $2-3$ centimetres with both methods.

3.3. Ultrasonic test results

3.3.1. P-wave and R-wave velocities

The time of flight (TOF) for the first wave packet, which may represent either direct P-waves or a combination of direct and refracted P-waves if refraction conditions are satisfied, is shown in Fig. 7(a)–(b) for concrete and mortar, respectively. The TOF curves for the first arrivals clearly distinguish the different materials and test conditions: thermal exposure (red and orange) or intact condition (black), and saturated (blue markers) or ambient conditions. As expected, the TOF is shorter for intact concrete compared to intact mortar. For both materials, the intact surfaces show shorter TOF than the thermally damaged surfaces, and water saturation further decreases the TOF compared to ambient moisture conditions.

The P-wave inversion results using a bi-layer refraction model are presented in Fig. 8(a)–(b) for concrete and mortar, respectively. As expected, the inverted P-wave velocities before saturation are higher in intact concrete than in intact mortar. The difference in P-wave velocities is attributed to the presence of limestone aggregates, which exhibit higher velocities than mortar, with values reported in the literature ranging from 3800 to 6500 m/s [44]. A low-velocity layer, approximately 1.2 cm thick, is observed near the surface of both intact concrete and mortar blocks, with a velocity decrease of 11% for concrete and 5% for mortar. This decrease in near-surface velocity could be due to surface drying caused by exposure to ambient laboratory environmental conditions, leading to a reduction in moisture content in the surface layer. The wall effect likely also contributes for concrete (estimated

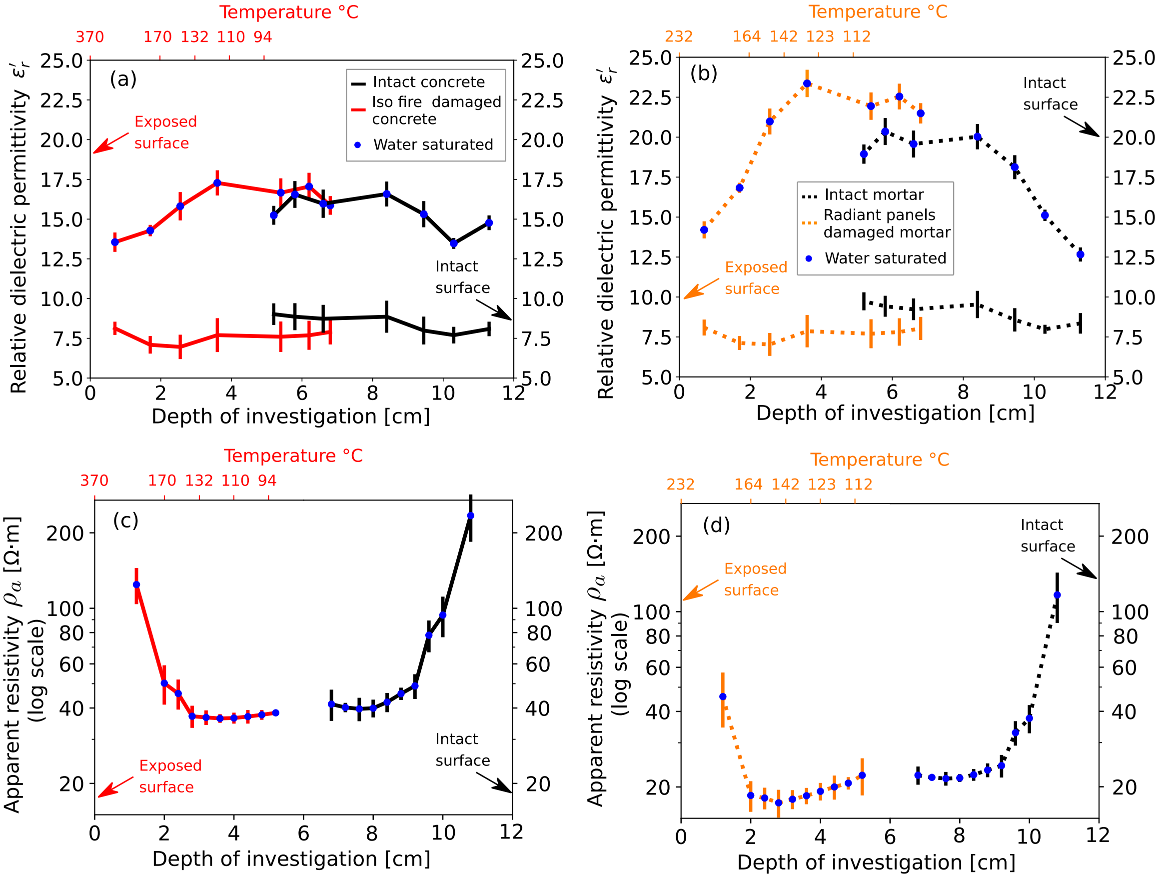

Fig. 5. Raw capacitance and DC-resistivity measurements on concrete and mortar blocks, before and after water saturation and curing, and on exposed and intact surfaces as function of investigation depth and temperature reached at each depth: (a) and (b) show the relative dielectric permittivity of concrete and mortar, respectively, with error bars indicating the standard deviation of nine measurements per probe. Investigation depths, estimated numerically, range from 0.7 cm (PE1) to 6.8 cm (GE2). (c) and (d) present apparent resistivity results for concrete and mortar, respectively; error bars represent the standard deviation of the mean at each level in the Schlumberger configuration. The exposed surface corresponds to 'depth = 0 cm', and the intact surface to 'depth = 12 cm'.

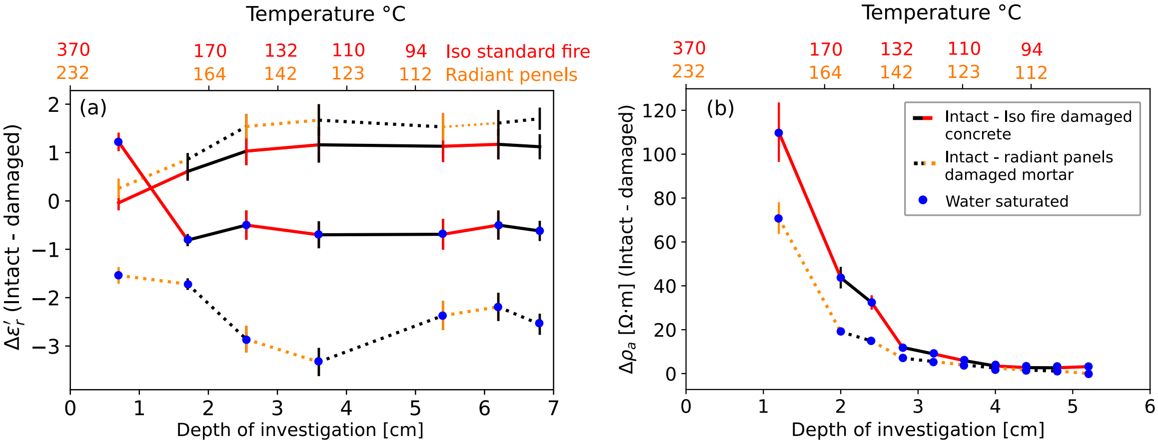

Fig. 6. Differential comparison of electromagnetic results between intact and thermally exposed surfaces before and after water saturation and curing, as a function of investigation depth and the temperature reached at each depth for each material block: (a) shows the difference in apparent dielectric permittivity, $\Delta\varepsilon'$, and (b) presents the difference in apparent resistivity, $\Delta\rho$.

depth: 8.4 mm) but not for mortar as its estimated depth (2.5 mm) is smaller.

Thermal exposure reduced velocities in both materials at slightly different rates. The damaged layer shows a P-wave velocity decrease of 14% in concrete and 13% in mortar.

The thickness of this damaged layer is approximately 1.7 cm for both materials. Since capacitive measurements have shown that water content of intact and exposed surfaces is similar at day 0, the reduction in wave velocity is attributed to changes in material microstructure. After water saturation, the conditions necessary for refraction were not satisfied in mortar, either on the surface exposed to radiant panels or

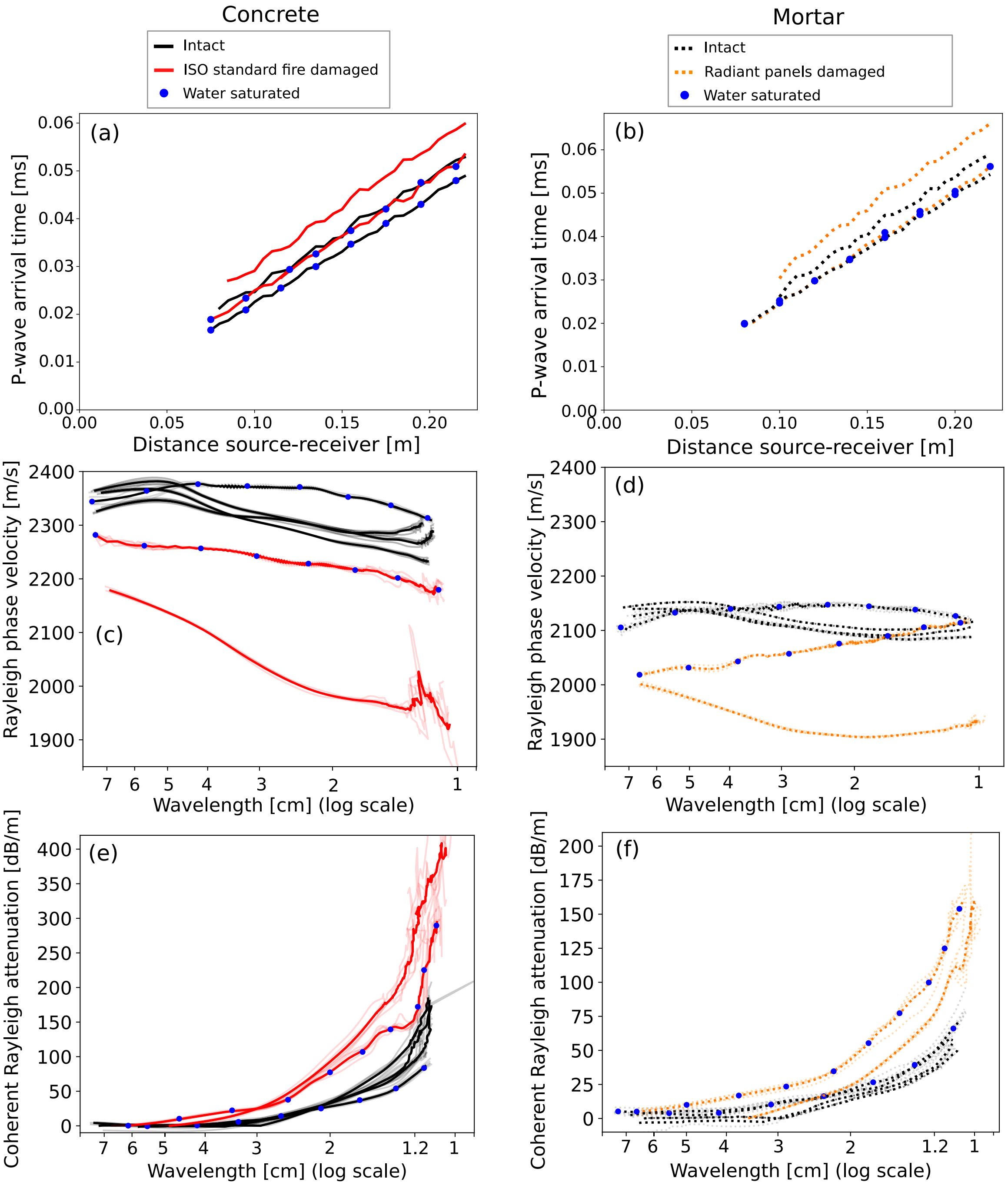

Fig. 7. Ultrasonic R-wave and P-wave measurement results on concrete and mortar blocks, on intact and exposed surfaces before and after water saturation and curing: (a) and (b) show the time of first P-wave arrivals as a function of source–receiver distance for concrete and mortar, respectively. (c) and (d) present R-wave phase velocity as a function of wavelength for concrete and mortar, respectively. (e) and (f) illustrate changes in R-wave coherent attenuation as a function of wavelength for concrete and mortar, respectively. The three black curves in (c-f) represent results from the two surfaces of the intact blocks and the unexposed surface of the damaged block. (For interpretation of the references to colour in this figure legend, the reader is referred to the web version of this article.)

on the intact surface. This suggests that the velocity remains relatively constant or decreases with depth. This behaviour is consistent with variations in the inverted shear wave velocities, as shown in Fig. 8(d), in which we observe a decrease in velocity with increasing wavelength (or penetration depth). The inverted results show that the P-wave velocity increases in both layers after water saturation, although at different rates. This increase is due to replacing air with water, as the sound velocity in water (approximately 1400 m/s) is significantly higher than in air (approximately 343 m/s). In the intact blocks, the direct P-wave velocity increases by approximately 13% and 8% in the first layer of concrete and mortar, respectively. For the damaged surface, the increase reaches approximately 17% for concrete subjected to ISO standard fire and 14% for mortar exposed to radiant panels. These tend to indicate that concrete absorbs more water than mortar, despite the higher cement paste content in mortar. This can be explained by a greater density of microcracks in the concrete, caused by the presence of aggregates and the intense thermal gradient associated with ISO standard fire exposure. Another factor contributing to the increase in velocity could be the changes in the microstructure caused by post-fire rehydration products. These products fill the microcracks, thereby reducing both the density of microcracks and the overall porosity.

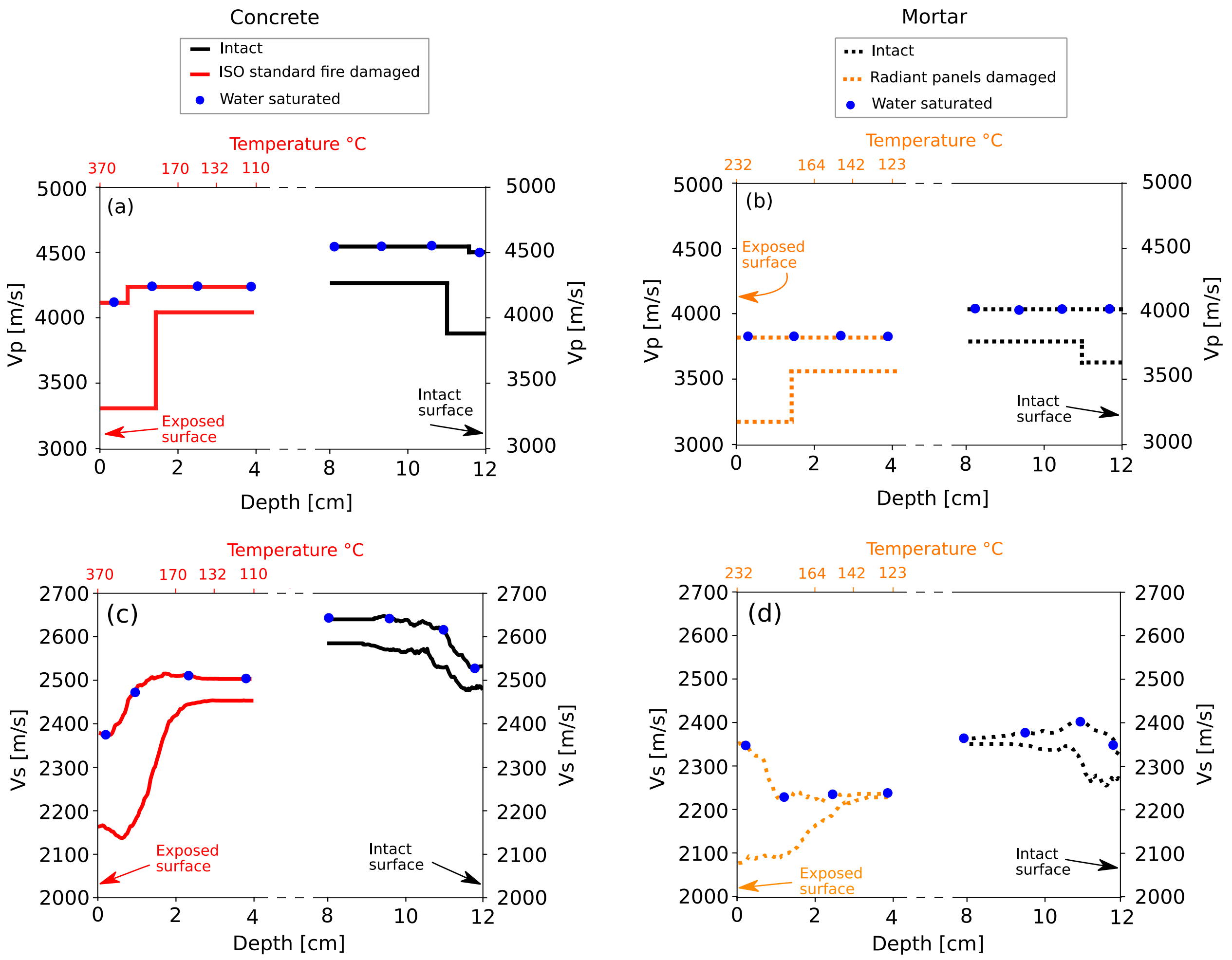

Fig. 8. Inversion results from ultrasonic R-wave and P-wave measurements on concrete and mortar blocks, on exposed and intact surfaces before and after water saturation and curing, as a function of depth and the temperature reached at each level: (a) and (b) show refracted P-wave inversion results using a bi-layer model, for concrete and mortar, respectively. (c) and (d) illustrate the inverted shear wave velocity (V_s) profiles for concrete and mortar blocks, respectively.

The experimental R-wave phase velocity curves as a function of wavelength are presented in Fig. 7(c)–(d) for concrete and mortar, respectively. The three black curves in each figure, shown as solid lines for concrete and as dotted lines for mortar, include the results for the two surfaces of the intact reference concrete block, as well as the velocity curve corresponding to the intact surface of the thermally damaged block (see Fig. 1(c)). This shows the variability in the production of concrete between specimens, as observed through ultrasonic measurements, even though the material comes from the same mix. At the same wavelength, a difference of up to 80 m/s, representing approximately 4%, is observed for concrete, and 35 m/s, approximately 2%, for mortar. The corresponding dispersion curves as a function of frequency are shown in Appendix A

As for P-wave, R-wave phase velocity curves are clearly distinct depending on the damages, moisture condition and material. As expected, the phase velocity is higher in concrete than in mortar by about 9%. At $\lambda = 2$ cm, a 14% decrease in velocity is observed in ISO-standards fire-damaged concrete compared to intact concrete, while a similar 10% decrease is noted for mortar exposed to radiant panels. These reductions in velocity are attributed to the increased density of microcracks since water content is similar in either surface.

Distinct trends in phase velocity are observed for both thermally damaged concrete (red solid curve) and mortar (orange dotted curve) in the range $\lambda \approx 2$ to $\lambda \approx 4$ cm. They correspond to the sharp variations in the inverted shear wave velocities shown in Fig. 8(c)–(d). To compare the extent of the two damages, we measure their characteristic depth as 80% of the difference between the surface velocity and the average velocity from 2 to 4 cm. With this definition, we obtain 1.3 cm for concrete exposed to ISO standard fire and 1.8 cm for mortar exposed to radiant panels.

As expected, R-wave velocity increases in saturated conditions. The effect is moderate for intact surfaces: 0 to 4% for concrete, 0 to 7% for mortar, depending on the wavelength. The damaged surfaces respond however much more: up to 12% for concrete and to 10% for mortar.

The post-saturation phase velocity curve for damaged concrete (solid red curve with blue markers) is similar in shape to the dispersion curve for intact concrete (solid black with blue markers), although thermal exposure reduces phase velocity by approximately 6% throughout the depth. The remaining gradient (see Fig. 8-(c)) appears similar to that of the intact surface, indicating a dominant sensitivity to water saturation effects. From this inverted data, one can wonder whether the mechanical properties of the saturated damaged surface are close to the intact ones. We will see later on that the (coherent) attenuation properties remain clearly distinct, hinting on that the surfaces are indeed still very different.

The effects of saturation in mortar are perhaps more surprising. Indeed, Fig. 7(d) shows that after saturation, the trend in phase velocity

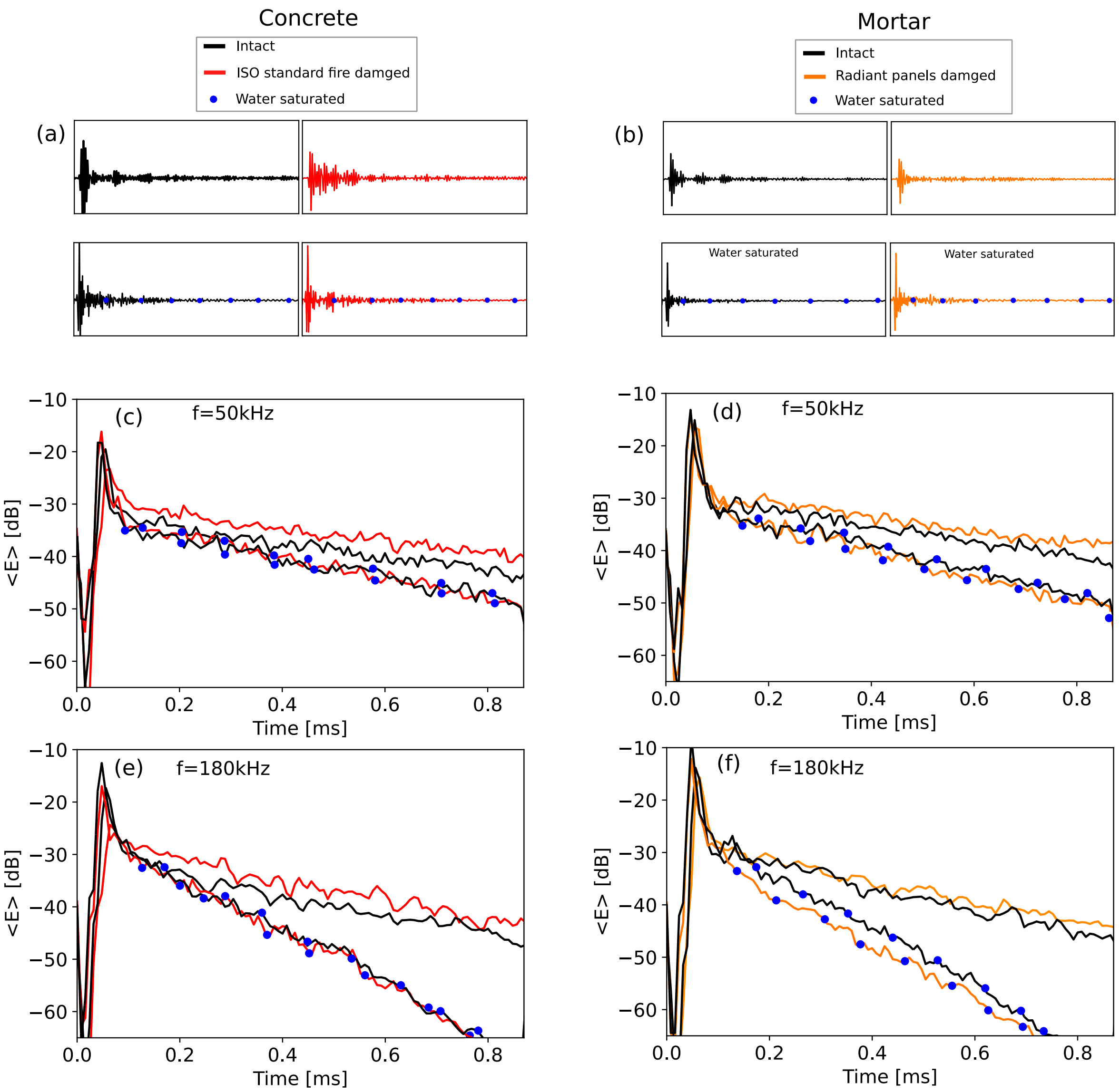

Fig. 9. Experimental results of signal energy density measurements at different frequencies, distances, and case studies for concrete and mortar blocks, on exposed and intact surfaces before and after water saturation and curing: (a) and (b) show time-domain signals recorded at a 5 cm source–receiver distance; (c) and (d) present energy density as a function of time, $\langle E(f,t)\rangle$, for a central frequency of 50 kHz, and (e) and (f) for 180 kHz, for concrete and mortar, respectively.

in both intact and radiant panel-damaged mortar is reversed, as velocity increases with shorter wavelengths. This translates into a “fast-to-slow” gradient, where velocity decreases with depth (see Fig. 8-(d)). This is possibly due to a high concentration of near-surface pores and cracks now filled with water (high moisture content) or rehydrated products that restore the microstructure (post-fire curing recovery). This trend is not observed in intact concrete or ISO standard-fired concrete, where an increase in velocity with depth is noted after saturation, but not to the extent of reversing the gradient trend. One possible reason is the material gradient due to the wall effect, which is prominent with a decreasing density of aggregates near the surface. From the comparison of velocities in intact mortar and concrete, we can estimate the effect of aggregates of about 13%. This figure is bigger than the 8% increase due to water saturation in mortar. This suggests that aggregate density remains the dominant factor over water content and gives an explanation of why this reversed gradient is not observed in concrete.

3.3.2. Rayleigh wave attenuation

The attenuation results are analysed in two categories: (i) coherent attenuation (c-attenuation), obtained from coherent field, and (ii) incoherent attenuation (inc-attenuation), obtained from incoherent field. Coherent attenuation is presented as a function of wavelength in Fig. 7(e)–(f) and as a function of frequency in Appendix B. Incoherent attenuation is shown in Figs. 9 and 10.

As expected, c-attenuation in both concrete and mortar generally increases with frequency under all conditions, whether the samples are damaged or intact, saturated or unsaturated. We observe that c-attenuation is higher in concrete than in mortar. For example, Fig. 7(e)–(f) shows attenuation values of about 120 dB/m at $\lambda = 1.2$ cm for intact concrete (matching the maximum aggregate size), compared to 60 dB/m for intact mortar at the same wavelength. This increase in c-attenuation with frequency highlights the sensitivity of R-waves to the

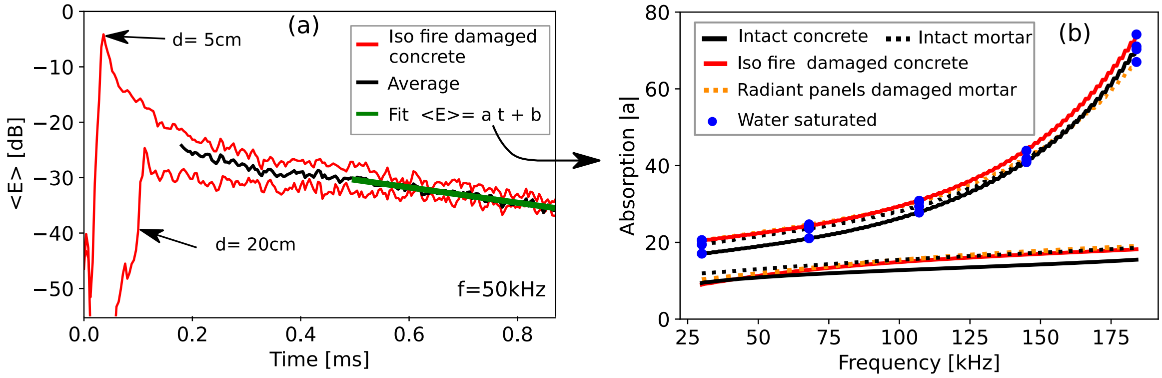

Fig. 10. Absorption $|a|$ of the incoherent field (incoherent attenuation): (a) shows an example of the processing applied to ISO-standard fire-exposed concrete at 50 kHz; (b) presents the estimated ultrasonic absorption as a function of frequency, comparing exposed and intact surfaces before and after water saturation and curing.

microstructural and viscoelastic properties of the tested materials. However, interpreting this relationship is complex, as it involves contributions from multiple processes, including scattering from heterogeneities and intrinsic attenuation due to the material's viscoelasticity.

C-attenuation increases dramatically after thermal damages. At $\lambda = 1.2$ cm, concrete results exhibits an increase of approximately 210 dB/m (196%) due to exposure to standard fire, whereas mortar exhibits an increase of 40 dB/m (98%) when exposed to radiant panels at the same wavelength, compared to the measurements on the intact surfaces.

Let us now examine the effect of water saturation (lines with blue dots). It is striking how small the effect is on concrete: at the same wavelength ($\lambda = 1.2$ cm), c-attenuation in damaged concrete decreased by only 30 dB/m (10%). The fact that the wavelength seems to be the dominating parameter (this is not the case of the frequency, see Appendix A) suggests that scattering is the primary cause of c-attenuation within this wavelength range. The slight decrease after 140 days of saturation might be due to the still ongoing post-fire re-curing effect, as indicated by the trend in Fig. 4(h): rehydrated products partially fill some cracks, improving the matrix/aggregate interfaces and thereby reducing the contribution of scattering. However, it seems that these interfaces still more closely resemble those of the damaged surface before re-curing than those of the intact one, which is a qualitatively different conclusion from what might be inferred from a velocity analysis alone.

Interestingly, an opposite effect of water saturation is observed in damaged mortar: at $\lambda = 1.2$ cm c-attenuation increased by 20 dB/m (21%). Our interpretation for this reversed trend compared to concrete is that, because of the smaller size of aggregates, the scattering effect is much less in this range of wavelengths to a point where material damping becomes a significant factor. Indeed, moisture is known to be a leading parameter for sound absorption in rocks, with wet rocks being more attenuative. Anticipating the inc-attenuation analysis, this is also the case here. Finally, we note that although the effect of water on c-attenuation in mortar is more noticeable, there is still a very clear distinction between intact and damaged surfaces, whatever their state of saturation.

In summary, the results of c-attenuation indicate a dominance of thermal damage contribution than to water content in concrete, with the curves under ambient and water saturated conditions showing a clear distinction between the damaged and intact surfaces. The slight variations observed after water saturation are attributed to post-fire re-curing recovery and absorption effects.

Let us now discuss the inc-attenuation. Because the blocks are isolated from neighbouring media (the impedance contrast with air is huge), the only source of inc-attenuation is material absorption. Absorption refers to various mechanisms that convert vibrational energy into heat through friction, fluid flow, and thermal relaxation processes. Studies on rocks in the frequency range of 0.1–1 MHz [45] have shown that friction at grain boundaries and within thin cracks is the main mechanism for inc-attenuation. Measurements under varying pressures demonstrate that inc-attenuation drops with higher pressure due to reduced friction. However, the presence of water increases inc-attenuation by wetting crack surfaces and grain boundaries, which facilitates frictional sliding through lubrication.

Examples of signals at a 5 cm source-receiver distance are shown in Fig. 9(a)–(b), respectively, for concrete (left) and mortar (right). The evolution of diffuse energy $\langle E(f,t)\rangle$ (at longer times) is shown in Fig. 9(c)–(d) for a frequency of, 50 kHz and in Fig. 9(e)–(f) for a frequency of 180 kHz. It can be observed that the energy of the incoherent component decays exponentially and attenuates more significantly under water saturation conditions and at higher frequencies (shorter wavelengths). It is also noted that the evolution and quantity of energy in the incoherent component appear to be insensitive to the material type or its damage state, but rather to its water content.

The incoherent attenuation (inc-attenuation) is determined by fitting an exponential function to the long-time decay, after averaging over distance, as shown in Fig. 10(a). This method applies over the frequency range of 30 to 180 kHz to analyse the evolution of absorption as a function of frequency. The results appear in Fig. 10(b). Inc-attenuation results confirm that energy loss in the incoherent component is predominantly influenced by water content rather than thermal damage or post-fire re-curing recovery effects. It effectively identifies the presence or absence of moisture but does not distinguish between damage levels or material types. Additionally, the results suggest that the initial water content of exposed and intact surfaces before saturation is nearly identical. This observation aligns with previous findings from electromagnetic capacitance measurements.

The key findings of the attenuation analysis can be summarized as follows:

(a) Coherent attenuation (c-attenuation) generally increases with frequency under all conditions, with concrete showing higher c-attenuation than mortar.
(b) Thermal damage leads to a significant increase in c-attenuation, particularly in ISO standard fired concrete.
(c) Water saturation slightly reduces c-attenuation in concrete but increases it in damaged mortar.
(d) Incoherent attenuation (inc-attenuation) is primarily governed by material absorption and is sensitive to water content. It increases with water saturation, especially at higher frequencies.
(e) The energy decay in the incoherent component is found to be independent of the material type and its damage state, being predominantly influenced by the moisture content.

4. Conclusions

Ultrasonic waves provide a non-destructive method for mapping mild to moderate thermal damage in cementitious materials. However, the combined influence of damage and moisture gradients on ultrasonic measurements remains unclear, even though it is known that rehydration partially restores mechanical properties. To address this knowledge gap, concrete and mortar blocks submitted to two distinct thermal exposures were inspected using ultrasounds and electromagnetic methods, first under ambient moisture conditions and subsequently under water saturation.

We found that ultrasonic velocities are sensitive to microstructural changes caused by thermal damage but are also strongly influenced by moisture content and recovery effects. On the other hand, attenuation analysis enables the separation of damage and moisture content effects using both coherent and incoherent components. Incoherent attenuation distinguishes the presence or absence of moisture but does not differentiate damage or material type, similar to electromagnetic methods. High absorption is associated with a high moisture content. Conversely, coherent attenuation demonstrates high sensitivity to thermal damage in the microstructure and is weakly (concrete) to moderately (mortar) affected by moisture. Resulting of this selective sensitivity, exposed and intact surfaces of either materials remained strongly differentiable even after 140 days of water saturation and post-fire curing recovery, while appearing much less different in terms of ultrasonic velocities.

Overall, the present study demonstrates the efficiency of Rayleigh wave attenuation in distinguishing the effects of thermal damage from those of moisture content. Attenuation can be used for non-destructive evaluation, complementing velocity, to assess the contribution of moisture content to the gradient of mechanical properties. Another novel use could be to monitor long-term post-fire recovery non-destructively without the need to dry the samples to separate the effects of moisture from recovery.

CRediT authorship contribution statement

Massina Fengal: Writing – review & editing, Writing – original draft, Visualization, Validation, Software, Resources, Methodology, Investigation, Formal analysis, Data curation. **Pierric Mora:** Writing – review & editing, Writing – original draft, Validation, Supervision, Software, Resources, Project administration, Methodology, Investigation, Funding acquisition, Formal analysis. **Parisa Shokouhi:** Writing – review & editing, Writing – original draft, Validation, Supervision, Methodology, Formal analysis. **Olivier Durand:** Writing – review & editing, Writing – original draft, Visualization, Software, Resources. **Xavier Dérobert:** Writing – review & editing, Writing – original draft, Validation, Software, Resources, Funding acquisition, Formal analysis. **Sérgio Palma-Lopes:** Writing – review & editing, Writing – original draft, Validation, Software, Funding acquisition, Formal analysis. **Maximilien Lehujeur:** Writing – review & editing, Writing – original draft, Software, Formal analysis. **Géraldine Villain:** Writing – review & editing, Writing – original draft, Validation, Methodology, Investigation, Formal analysis. **Eric Gennesseaux:** Writing – review & editing, Writing – original draft, Resources, Methodology, Funding acquisition. **Odile Abraham:** Writing – review & editing, Writing – original draft, Visualization, Validation, Supervision, Resources, Project administration, Methodology, Investigation, Funding acquisition, Formal analysis, Conceptualization.

Declaration of competing interest

The authors declare the following financial interests/personal relationships which may be considered as potential competing interests: Massina FENGAL reports financial support was provided by Regional Council of Pays de la Loire. Pierric Mora reports financial support was provided by Regional Council of Pays de la Loire. If there are other authors, they declare that they have no known competing financial interests or personal relationships that could have appeared to influence the work reported in this paper.

Acknowledgements

The authors gratefully acknowledges the funding support for Gustave Eiffel university and Regional Council of Pays de la Loire. The authors are thankful to Pierre Pimienta, Roberto Fellicetti and Cédric Payan for insightful discussions.

Appendix A. Rayleigh wave raw and inverted results

The experimental R-wave phase velocity and coherent attenuation curves as a function of frequency are presented in Fig. A.11 for concrete and mortar.

This representation is more usual and closer to raw measurements than Fig. 7 as it does not include the conversion from frequency to wavelength, but it is also less instructive since penetration depths are not readily comparable. Therefore, interpreting the results based on wavelength is more appropriate. When plotted against frequency, coherent attenuation in concrete (Fig. A.11(a)) is dependent upon moisture.

Fig. A.12 illustrates the inversion results for an intact concrete surface under ambient moisture conditions. The left panel depicts the model space, with dashed black lines marking the boundaries of the search area. The coloured shear wave velocity (V_S) models represent the 1000 best solutions, while the thick grey line denotes their median. The right panel presents the fundamental mode Rayleigh wave phase velocities (RC0), where the coloured curves correspond to the dispersion curves of the 1000 best models, with colours indicating log-likelihood values. The red curve represents the observed Rayleigh wave phase velocity dispersion data used in this inversion.

Appendix B. Refracted P-wave inversion

Fig. B.13 illustrates the processing procedure for refracted P-wave measurements. First-arrival picking (b) was performed on the B-scan (a), with travel times determined as the average from 50 data measurements. The resulting curves were then fitted using a bi-layer refraction model. The refraction principle is illustrated in (c) for a single-layer system of thickness e_1, with a longitudinal P-wave velocity V_1, overlying an infinite medium with a P-wave velocity V_2, where $V_2 > V_1$. For an incident angle exceeding the critical angle $\alpha = \arcsin\left(\frac{V_1}{V_2}\right)$, the refracted wave does not propagate into the infinite medium, but instead travels along the interface. The determination of V_1, e_1, and V_2 requires information on the arrival times of the longitudinal P-wave as a function of the source-receiver distance. The fitting procedure, along with an application example on an intact concrete block under ambient moisture conditions, is shown in (d).

Data availability

Data will be made available on request.

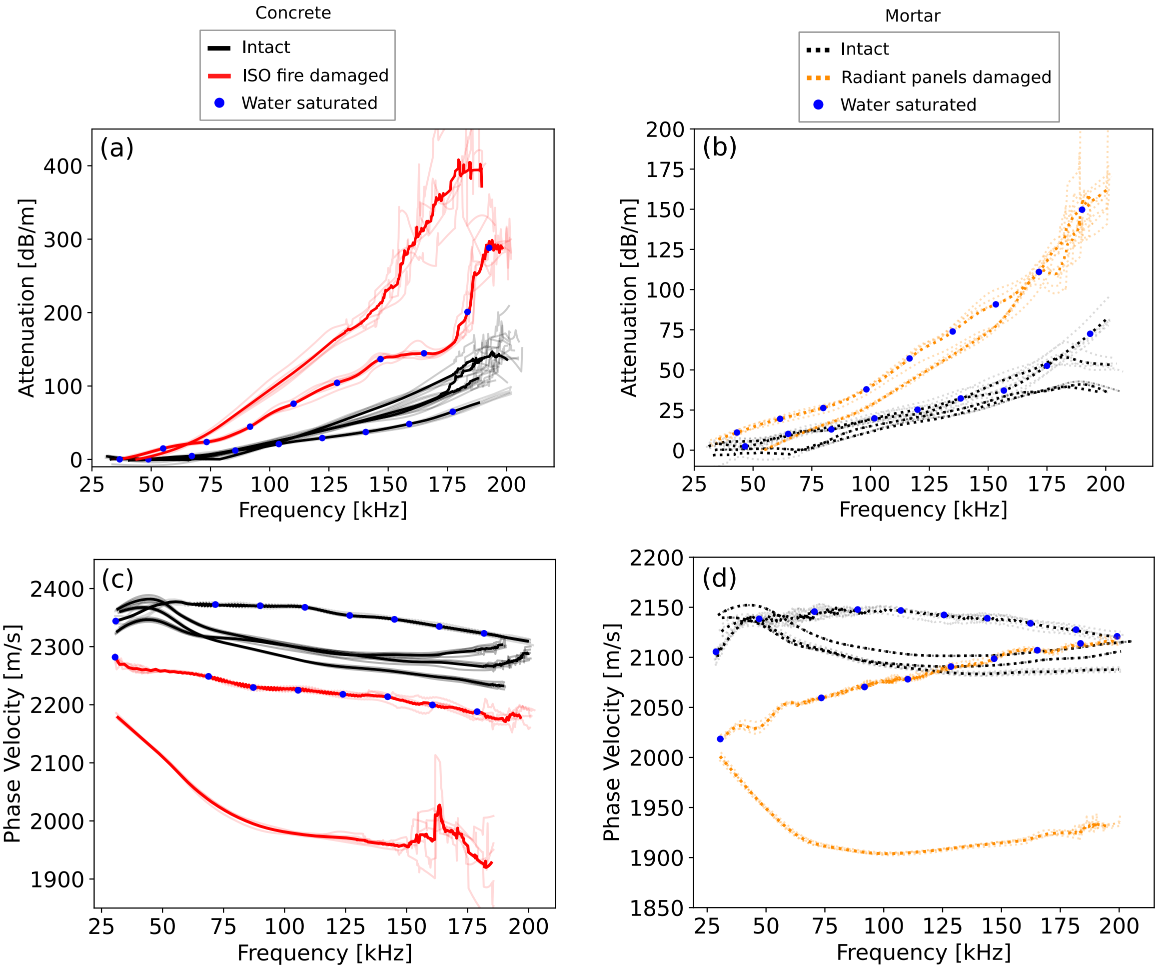

Fig. A.11. Ultrasonic R-wave measurement results on concrete and mortar blocks, on intact and exposed surfaces before and after water saturation and curing: (a) and (b) illustrate changes in R-wave coherent attenuation as a function of frequency for concrete and mortar, respectively. (c) and (d) present R-wave dispersion curves for concrete and mortar, respectively. The three black curves represent results from the two surfaces of the intact blocks and the unexposed surface of the damaged block. (For interpretation of the references to colour in this figure legend, the reader is referred to the web version of this article.)

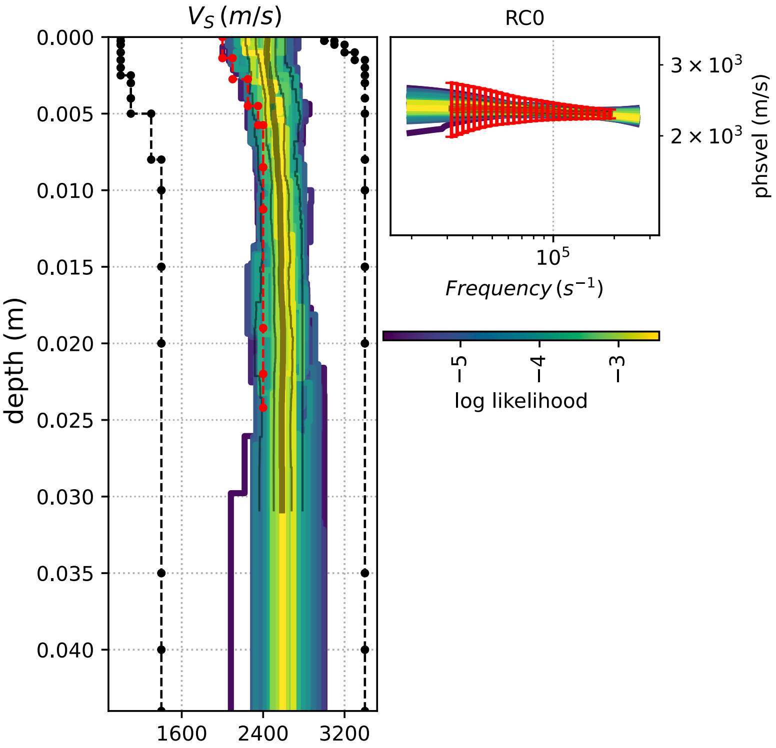

Fig. A.12. Inversion results for an intact concrete surface under ambient moisture conditions: (Left panel) Model space, where the dashed black lines indicate the boundaries of the search area. The coloured V_S models correspond to the 1000 best solutions, with the thick grey line representing their median. (Right panel) RC0 correspond to the phase velocities of the fundamental mode Rayleigh waves. The coloured curves correspond to the dispersion curves of the 1000 best models, colours correspond to log-likelihood values; The red curve with error bars shows the observed Rayleigh wave phase velocity dispersion data inverted in this example. (For interpretation of the references to colour in this figure legend, the reader is referred to the web version of this article.)

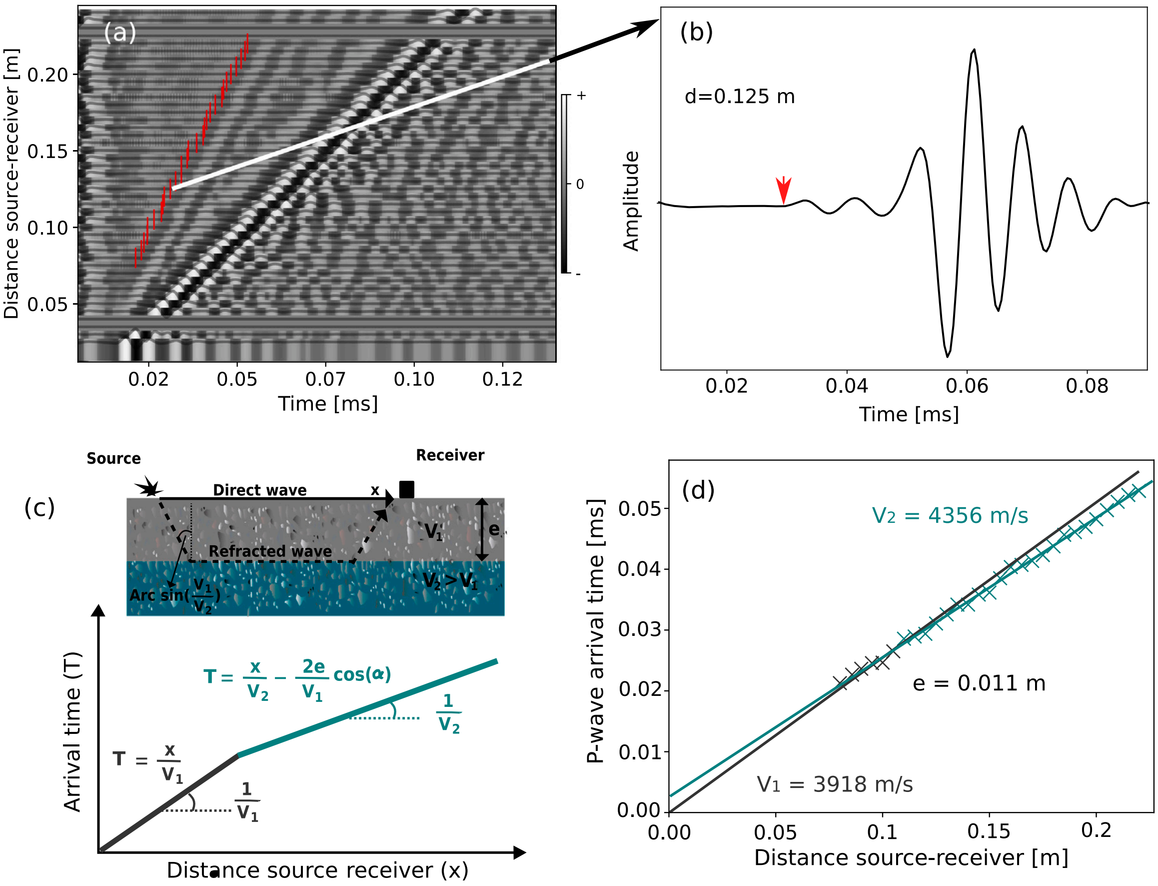

Fig. B.13. Processing procedure for refracted P-wave measurements on an example of an intact concrete block under ambient moisture conditions: (a) and (b) present first-arrival picking results; (c) illustrates the principle of P-wave refraction, including a description of the medium and the measurement setup; (d) shows an application of this model to data acquired from the intact surface of a concrete block under ambient moisture conditions.

References

[1] Schneider U. Concrete at high temperatures—a general review. Fire Saf J 1988;13(1):55–68.

[2] Colombo M, Felicetti R. New NDT techniques for the assessment of fire-damaged concrete structures. Fire Saf J 2007;42(6–7):461–72.

[3] Georgali B, Tsakiridis P. Microstructure of fire-damaged concrete. a case study. Cem Concr Compos 2005;27(2):255–9.

[4] Pulkit U, Adhikary SD. Effect of micro-structural changes on concrete properties at elevated temperature: current knowledge and outlook. Struct Concr 2022;23(4):1995–2014.

[5] Büyüköztürk O, Taşdemir MA, Felicetti R. Assessment of fire damaged concrete via the hammer-drill pulse transmission technique. In: Nondestructive testing of materials and structures. Elsevier; 2013, p. 205–12.

[6] Chekroun M, Le Marrec L, Abraham O, Durand O, Villain G. Analysis of coherent surface wave dispersion and attenuation for non-destructive testing of concrete. Ultrasonics 2009;49(8):743–51.

[7] Abraham O, Dérobert X. Non-destructive testing of fired tunnel walls: the Mont-Blanc tunnel case study. NDT & E Int 2003;36(6):411–8.

[8] Felicetti R. Assessment of a fire-damaged concrete overpass: the Verona bus crash case study. J Struct Fire Eng 2022;13(3):293–306.

[9] Du Plooy R, Lopes SP, Villain G, Derobert X. Development of a multi-ring resistivity cell and multi-electrode resistivity probe for investigation of cover concrete condition. NDT & E Int 2013;54:27–36.

[10] Dérobert X, Iaquinta J, Klysz G, Balayssac J-P. Use of capacitive and GPR techniques for the non-destructive evaluation of cover concrete. Ndt & E Int 2008;41(1):44–52.

[11] Sánchez I, Antón C, De Vera G, Ortega JM, Climent M. Moisture distribution in partially saturated concrete studied by impedance spectroscopy. J Nondestruct Eval 2013;32:362–71.

[12] Balayssac J-P, Laurens S, Arliguie G, Breysse D, Garnier V, Dérobert X, et al. Description of the general outlines of the french project SENSO–quality assessment and limits of different NDT methods. Constr Build Mater 2012;35:131–8.

[13] Fares M, Fargier Y, Villain G, Derobert X, Lopes SP. Determining the permittivity profile inside reinforced concrete using capacitive probes. NDT & E Int 2016;79:150–61.

[14] Abraham O, Piwakowski B, Villain G, Durand O. Non-contact, automated surface wave measurements for the mechanical characterisation of concrete. Constr Build Mater 2012;37:904–15.

[15] Popovics S. Effects of uneven moisture distribution on the strength of and wave velocity in concrete. Ultrasonics 2005;43(6):429–34.

[16] Soltani F, Goueygou M, Lafhaj Z, Piwakowski B. Relationship between ultrasonic Rayleigh wave propagation and capillary porosity in cement paste with variable water content. NDT & E Int 2013;54:75–83.

[17] Candelaria MDE, Kee S-H, Yee J-J, Lee J-W. Effects of saturation levels on the ultrasonic pulse velocities and mechanical properties of concrete. Materials 2020;14(1):152.

[18] Karastathis VK, Karmis PN, Drakatos G, Stavrakakis G. Assessment of the dynamic properties of highly saturated concrete using one-sided acoustic tomography. Application in the marathon dam. Constr Build Mater 2002;16(5):261–9.

[19] Ohdaira E, Masuzawa N. Water content and its effect on ultrasound propagation in concrete—the possibility of NDE. Ultrasonics 2000;38(1–8):546–52.

[20] Zheng J, Li CQ, Jones M. Aggregate distribution in concrete with wall effect. Mag Concr Res 2003;55(3):257–65.

[21] Ren Q, Pacheco J, de Brito J. Calibration of wall effects in mesostructure modelling of concrete using marker-controlled watershed segmentation. Constr Build Mater 2023;398:132505.

[22] Landis EN, Shah SP. Frequency-dependent stress wave attenuation in cement-based materials. J Eng Mech 1995;121(6):737–43.

[23] Ichikawa Y, England GL. Prediction of moisture migration and pore pressure build-up in concrete at high temperatures. Nucl Eng Des 2004;228(1–3):245–59.

[24] Fu Y, Wong Y, Tang C, Poon CS. Thermal induced stress and associated cracking in cement-based composite at elevated temperatures—-Part I: Thermal cracking around single inclusion. Cem Concr Compos 2004;26(2):99–111.

[25] Malik M, Bhattacharyya S, Barai SV. Microstructural changes in concrete: Postfire sc enario. J Mater Civ Eng 2021;33(2):04020462.

[26] Alonso C, Fernandez L. Dehydration and rehydration processes of cement paste exposed to high temperature environments. J Mater Sci 2004;39(9):3015–24.

[27] Mukhopadhyay AK, Zollinger DG. Development of dilatometer test method to measure coefficient of thermal expansion of aggregates. J Mater Civ Eng 2009;21(12):781–8.

[28] Loser R, Münch B, Lura P. A volumetric technique for measuring the coefficient of thermal expansion of hardening cement paste and mortar. Cem Concr Res 2010;40(7):1138–47.

[29] Mokhtar TA, Herrmann R, Russell D. Seismic velocity and Q model for the shallow structure of the Arabian shield from short-period Rayleigh waves. Geophysics 1988;53(11):1379–87.

[30] Lehujeur M, Vergne J, Schmittbuhl J, Zigone D, Le Chenadec A, Team E. Reservoir imaging using ambient noise correlation from a dense seismic network. J Geophys Res: Solid Earth 2018;123(8):6671–86.

[31] Tikhonov AN. Solution of incorrectly formulated problems and the regularization method. Sov Dok 1963;4:1035–8.

[32] Forbriger T. Inversion of shallow-seismic wavefields: I. Wavefield transformation. Geophys J Int 2003;153(3):719–34.

[33] Breysse D. Non-destructive assessment of concrete structures: Reliability and limits of single and combined techniques: State-of-the-art report of the RILEM technical committee 207-INR. vol. 1, Springer Science & Business Media; 2012.

[34] Edwards L. A modified pseudosection for resistivity and IP. Geophysics 1977;42(5):1020–36.

[35] Poon C-S, Azhar S, Anson M, Wong Y-L. Strength and durability recovery of fire-damaged concrete after post-fire-curing. Cem Concr Res 2001;31(9):1307–18.

[36] Li L, Shi L, Wang Q, Liu Y, Dong J, Zhang H, et al. A review on the recovery of fire-damaged concrete with post-fire-curing. Constr Build Mater 2020;237:117564.

[37] Lin Y, Hsiao C, Yang H, Lin Y-F. The effect of post-fire-curing on strength–velocity relationship for nondestructive assessment of fire-damaged concrete strength. Fire Saf J 2011;46(4):178–85.

[38] Henry M, Darma IS, Sugiyama T. Analysis of the effect of heating and re-curing on the microstructure of high-strength concrete using X-ray CT. Constr Build Mater 2014;67:37–46.

[39] Pei Y, Agostini F, Skoczylas F. Rehydration on heat-treated cementitious materials up to 700°C-coupled transport properties characterization. Constr Build Mater 2017;144:650–62.

[40] Henry M, Darma IS, Haraguchi Y, Sugiyama T. Analysis of cracking in high-strength cementitious materials under heating and re-curing using X-ray CT. In: Third international conference on sustainable construction materials and technologies. Elsevier; 2013.

[41] Villain G, Le Marrec L, Rakotomanana L. Determination of the bulk elastic moduli of various concretes by resonance frequency analysis of slabs submitted to impact echo. Eur J Environ Civ Eng 2011;15(4):601–17.

[42] Du Plooy R, Villain G, Palma Lopes S, Ihamouten A, Derobert X, Thauvin B. Electromagnetic non-destructive evaluation techniques for the monitoring of water and chloride ingress into concrete: a comparative study. Mater Struct 2015;48:369–86.

[43] Hallikainen MT, Ulaby FT, Dobson MC, El-Rayes MA, Wu L-K. Microwave dielectric behavior of wet soil-part 1: Empirical models and experimental observations. IEEE Trans Geosci Remote Sens 1985;(1):25–34.

[44] Solís-Carcaño R, Moreno EI. Evaluation of concrete made with crushed limestone aggregate based on ultrasonic pulse velocity. Constr Build Mater 2008;22(6):1225–31.

[45] Johnston DH, Toksöz M, Timur A. Attenuation of seismic waves in dry and saturated rocks: Ii. mechanisms. Geophysics 1979;44(4):691–711.